LIP-STUDENTS-23-19

A Study on a 10-Double Gap RPC-Based Neutron Detector

Dinis Beleza[1], Daniel Marmelo[2], David Mendonça[3], Filipa Santos[2]

[1] University College London, London, United Kingdom
[2] University of Coimbra, Coimbra, Portugal
[3] University of Aveiro, Aveiro, Portugal

Project supervisors: Luís Margato; Andrey Morozov

November 2, 2023

Abstract. In this project, a study on a 10-Double Gap Resistive Plate Chamber Neutron Detector was performed. The objective was to understand how the detector was built and learn how the data was retrieved from it. Furthermore, simulations were performed to know whether this detector could be optimised in terms of detection efficiency and counting rate. These simulations were on the optimal angle of incidence of the neutron beam and the optimal converter thickness and it was shown that the optimal angle of incidence of the neutron beam is 5º and that the optimal converter thickness on the detector is 1.15 µm. Apart from this, different position reconstruction methods (strongest strip method, the centroid method and the statistical method) were studied to understand the advantages and disadvantages of each. This project was developed within the framework of the 'Laboratório de Instrumentação e Física Experimental de Partículas' Summer Internships focused on particle and detector investigation.

Keywords: Resistive-Plate Chambers, Neutron Detectors, Simulations

1 Introduction

Resistive Plate Chambers (RPC) lined with $^{10}B_4C$ are an emerging neutron detection technology. They offer sub-millimeter spatial resolution, sub-nanosecond timing accuracy, and good scalability to large areas at low cost [1], as well as an alternative to the classical ^3He detectors of this kind. Significant effort has recently been given to improve this technology. In particular, the European Spallation Source (ESS) is one of the large scale neutron facilities that is strongly involved in this investigation.

Sensitivity to thermal neutrons in a Boron-10 RPC detector is achieved through the neutron capture reaction of $^{10}B(n,\alpha)^7Li$ in $^{10}B_4C$ layers covering an aluminium plate, which creates α and Li particles. Previously, a single-gap 10B-RPC prototype in a hybrid configuration, in which cathodes are metallic, has been shown to be a feasible detection technology for thermal neutron detectors, giving spatial resolution better than 0.5 mm [2]. However, these detectors provide low detection efficiency when compared to ^3He-based ones [2]. There have been several attempts to improve these values, which included implementing a multilayer or inclined layer architecture relative to the neutron beam direction [1].

In this paper, we report on a new neutron detector with a multilayer design (ten double-gap RPCs in hybrid configuration, with 20 layers of $^{10}B_4C$ in total).

This prototype aims to achieve a detection efficiency above 60% and spatial resolution down to 0.25 mm. Across the next sections, a description of the neutron RPC detector and on the detector electronic readout is made. Furthermore, an explanation on how the cathode readout electronic channels were calibrated is also provided. Finally, this paper reports different reconstruction methods for XY positions and a simulation study on how detection efficiency depends on the converter thickness and angle of incidence of the neutron beam.

2 Neutron RPC Detector Concept

The central element of a double-gap hybrid RPC unit is an aluminium plate, acting as a cathode, which is coated by a thin $^{10}B_4C$ layer. On both sides lies float glass, acting as an anode. The gas gap between the cathode and the anodes is filled with tetrafluoroethane ($C_2H_2F_4$) and the gas gap width is maintained by the monofilament spacers (see Figure 1).

To organise the signal readout, a flexible printed circuit board (PCB) containing two orthogonal arrays of signal pickup strips is installed in front of each anode.

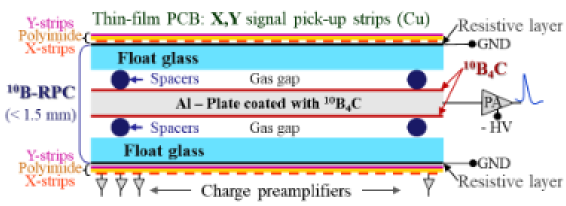

Figure 1. Schematic cross section view of a double gap $^{10}B-RPC$ (neutron RPC).

Neutron absorption by the Boron atom releases a pair of the charged particles (Li and α), which in turn results in primary ionisation. Due to the imposed electrical field on the gas gap, electron avalanches occur, leading to induction of charge in the arrays of pick-up electrodes. By measuring the distribution of the amplitude of the induced signals the position of each neutron event can be found. A detailed description of the detector concept can be found in [2].

In this type of detector, with solid neutron converters, there are two main alternatives to improve the detection efficiency: (1) use a multilayer configuration with the beam at normal incidence and (2) tilt the RPC with respect to the neutron beam by a small angle. In order to set up the multilayer configuration, the RPC units are stacked on top of each other (see Figure 2). More details regarding these two configurations can be found in [2]. For the following sections only the first one is considered.

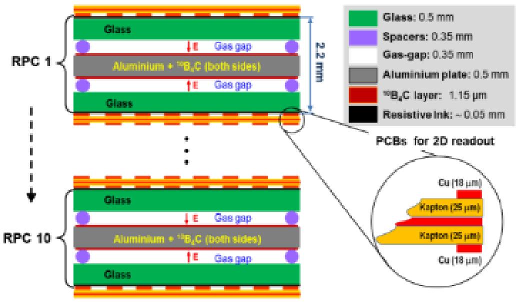

Figure 2. Schematic drawing of the multilayer RPC configuration.

3 Detector Prototype

3.1 Prototype Components

In Section 2 of this paper, we presented the conceptual design and working principles of a multilayer $^{10}B - RPC$ detector. The detector prototype, previously assembled at LIP laboratories, consists of a stack of ten ^{10}B–RPC detection units (described in the prior section), and is illustrated in Fig. 3.

Figure 3. Image of a $^{10}B - RPC$ detection unit.

To allow for the signal detection capabilities, a thin flexible multilayer printed circuit board (FPCB) with signal pickup strips is positioned between each adjacent module pair. The complete stacking of these detection units can be seen in Fig. 4.

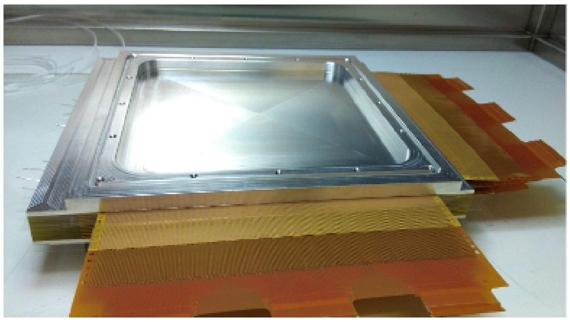

Figure 4. Thin flexible multilayer printed circuit boards (FPCBs) with ten $^{10}B - RPCs$ already assembled. The aluminium neutron entrance window is located at the top, while on the sides we can see the FPCBs with the X and Y signal pickup strips.

3.2 Electronic Readout

The detector prototype aims to provide precise position sensitivity and timing capability. This four-dimensional functionality implies simultaneous reading of both time and spatial coordinates (x, y, z) of the neutron events.
The FPCBs are used to readout the position of an event on the anode side. They are composed of two orthogonal sets, each containing 192 signal pickup strips. This enables the direct reading of X and Y coordinates, respectively.
Cathodes are read by fast amplifiers, allowing to identify the specific cathode where an event took place, giving the Z coordinate. Each cathode's output is divided into two branches: the slow signal induced by drift of the ions and the fast signal generated by the electrons. This last component is used to obtain the temporal coordinate, playing a crucial role in triggering the DAQ for starting data collection and, more importantly, determining the neutron's time-of-flight (TOF).
Once the fast signal's amplitude surpasses a certain threshold (10 mV in our case), a digital signal is generated (in this instance, LVDS) and employed by DAQ's programmable trigger system to register cathode trigger states. The threshold value was defined according to the electronic noise level.
Next, the FPCBs drive the signals from the strips to the Front-End Electronics (FEE) boards, each equipped with 24 charge-sensitive preamplifiers with a sensitivity of 50 mV/pC. This prototype features eight rows of connectors for each of the X and Y signals, with each row accommodating one FEE board.
To assemble the FEE boards, it was essential to electromagnetically isolate them using Faraday cages (copper-coloured plates seen in Figure 5), to prevent pickup noise and interference between them.

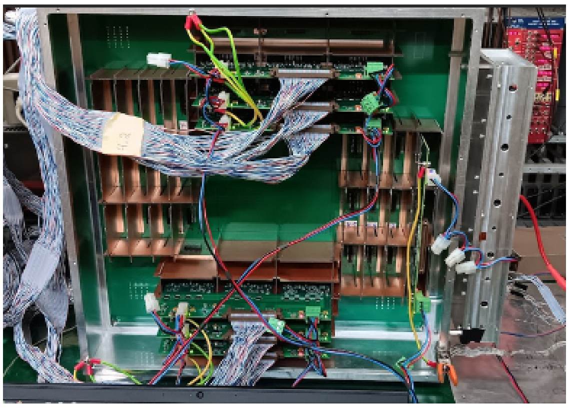

Figure 5. Image of the back side of the detector prototype, displaying the FEE boards plugged to the main PCB.

3.3 Data Acquisition System

The DAQ is a system based on the TRB3 readout system [3], and consists of six boards: two central boards, serving as the primary processing units for triggering and building events while simultaneously maintaining communication with the computer, and four additional boards equipped with analog-to-digital converter (ADC) addons. These central boards correspond to a 48-channel TRB3 module [4] with a TDC precision of 10 ps. On the other hand, each ADC addon is equipped with two 24-channel connectors (each connected to a FEE Board) and based on 40 MHz streaming ADCs.
In total, the prototype utilises $2 * 96$ DAQ channels for readout purposes. Among these channels, 5 channels from both the X and Y coordinates are allocated to read the 10 cathodes, while the remaining 91 channels of each coordinate are used to read the pickup strips. With a pitch of 1 mm between the strips, an area of approximately 90 mm x 90 mm can be read, which is only about 1/4 of the total area of the detector. The overall active area of the detector measures roughly 190 mm x 190 mm and would need 192 strips for each coordinate, however, only half of the channels were available for use.

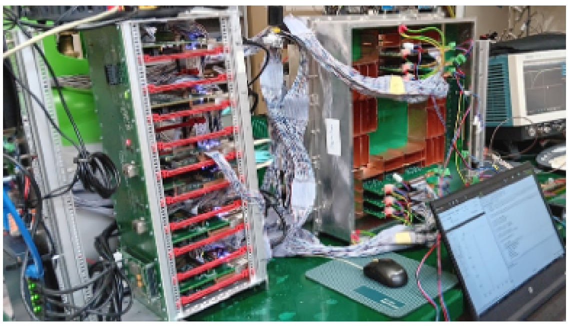

Figure 6. Photograph illustrating the full readout and DAQ setup with the cables driving the signals from the FEEs (on the right-hand side) to the DAQ system (left-hand side).

4 Calibration of the Cathodes Channels

One of the objectives of this study was to calibrate the cathode amplification channels of the 10 RPCs comprising the detector. Calibration is a critical process to ensure the accuracy and reliability of instruments, with particular emphasis on maintaining linearity. In this case, the focus was on calibrating the charge-sensitive pre-amplifiers (PAs) within the detector system. For a certain charge induced by the detector, it is crucial to know the sensitivity of the PAs, as it affects their output signal amplitude in relation to the input charge (Amplitude = Charge x Sensitivity). Although PAs may exhibit known gains, channel-specific corrections to identify discrepancies are needed to maintain the position resolution integrity.
To address this, a calibration process was undertaken, involving the injection of known charge through a capacitor ($Q = CV$). To ensure an accurate calibration, it is essential to have control over the input charge signal in the detector. This prompted the application of a pulsed signal directly to individual cathodes, instead of employing a neutron beam. Thus, the charge calibration setup involved using a pulse generator to supply a known charge by a calibrated capacitor. This charge then is sensed by the charge preamplifier (FEE channel) and was, subsequently, registered by the DAQ. Through consecutive adjustments of DAQ parameters related to signal sampling by ADC addons (e.g., buffer depth - the number of samples to acquire), the response of the pre-amplifiers (PAs) to the injected charges was optimised by analysing the resulting signal amplitudes.
In order to determine the amplitude of the signals, digital post-processing techniques (such as trapezoidal and adjacent averaging filters) were applied to rectify baseline variations and smooth the fluctuations in the signal's waveform. The distribution of the cathode signal amplitudes obtained for a dataset recorded, and subjected to the adjacent averaging filter can be seen in Fig. 7.

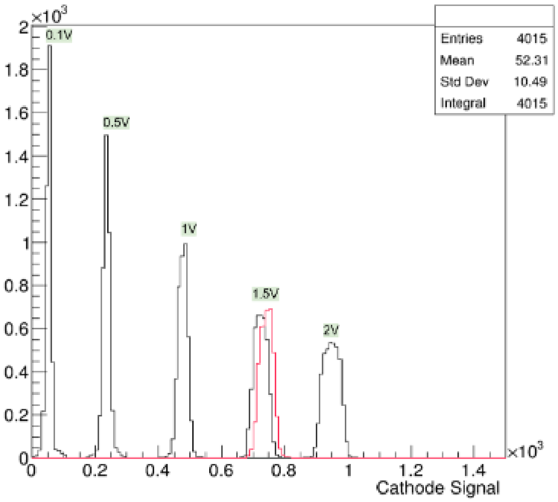

Figure 7. Distribution of the cathode signal amplitudes for increasing values of the applied voltage (V_{in}), shown in black for cathode number 10. The red curve represents the signal amplitude for cathode number 7 and displays a similar sensitivity when applying a tension of 1.5 V.

From these results, it is possible to observe that increasing the amplitude of the pulse generator signal directly correlates with the increase of the charge injected into the PA, and leads to an increase in the amplitude at the output of the PA. Furthermore, decreasing resolution was observed throughout the PA's dynamic range as the Full Width at Half Maximum (FWHM) values for each peak enlarged. While calibration was performed for only one electronics channel, the process should be applied across all channels to ensure consistent responses and verify if they exhibited comparable sensitivity across all the cathodes.

5 XY Position Reconstruction

To compare the performance of several algorithms for reconstruction of the neutron capture positions we have used the data that were recorded when the early prototype of the detector was taken to the V-17 beam line at Helmholtz-Zentrum Berlin. There, the mask from Figure 8 was placed at the detector's neutron entrance window and then normally irradiated with a neutron beam with very low divergence.

Figure 8. 0.25 mm thick gadolinium mask forming the letters "HZB" and a pictogram.

During our work, three methods to reconstruct images were studied, tested and the obtained results cross-compared with each other. Note that for all applied methods the reconstruction is performed independently for X and Y directions.

5.1 Strongest Strip Method

This method consists of setting the position of an event at the centre coordinate of the strip where the strongest signal is detected. The obtained image for the dataset with the mask described above is shown in Figure 9.

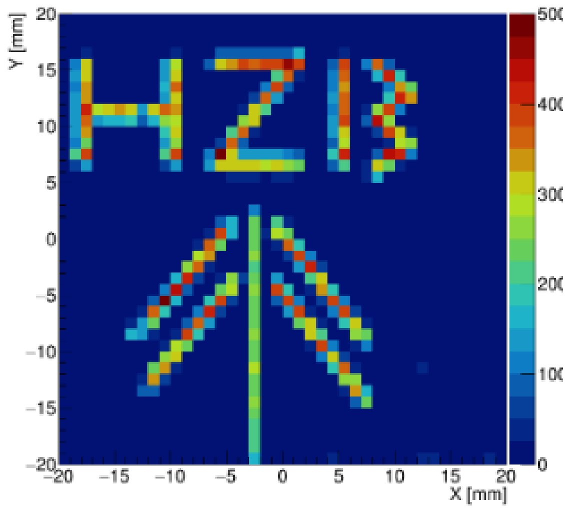

Figure 9. Reconstructed image obtained using the strongest strip approach (40 x 40 bins).

As expected, the image resolution is limited to the 1 mm pitch of the pick-up strips.

5.2 Centroid Method

For this method, the position on X (the same goes for Y) is given by:

$$X = \frac{\sum_i X_i S_i}{\sum_i S_i} \tag{1}$$

This expression is a weighted average performed over all strips of a single set (X or Y). As we can see in equation (1), the strip position, X_i, is weighted by the amplitude of the signal induced on it, S_i. The resulting image for the test dataset is shown in Figure 10.

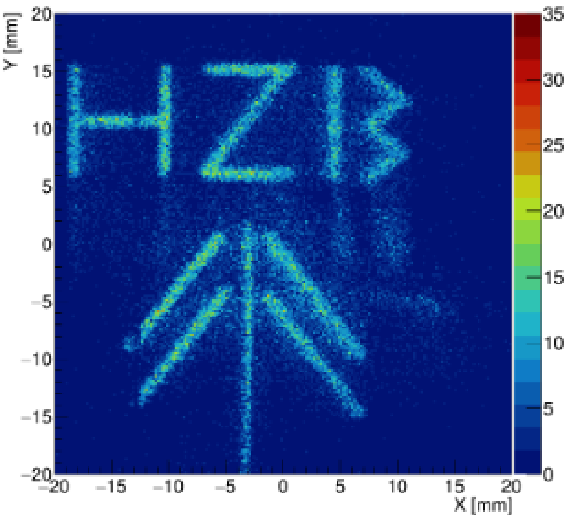

Figure 10. Reconstructed image obtained using the centroid approach (200 x 200 bins).

The image shows a high degree of distortions since the weighted average is performed over all available strips: it takes into account strips where random background noise is recorded and if some of these strips are distant enough, the event position will be set at an obviously incorrect position.
This naturally calls for an optimization in which we only take into account a certain number of strips instead of all of them.

5.3 Optimized Centroid Method

The optimization starts with finding the strip where the maximum signal is detected. Then, 4 strips are selected on each side of the strip with the maximum signal. If the signal on these strips is below 20 triggered ADC channels, the strip is not taken into account. After this, the position is calculated through equation (1), but only with the selected strips.
Some filtering is also applied. We skip events in which:

- The cathode signal is below 275 triggered ADC channels or above 4275 triggered ADC channels.
- The number of selected strips is less than 2.
- The ratio between the sum over all signals on X and the sum over all signals on Y is below 0.8 or above 2.8.
- The ratio between the two sums previously defined combined and the cathode signal is below 0.8 or above 2.5.

The thresholds for the cathode signal were applied in order to avoid taking noise and saturation into account. Their values were chosen after obtaining histograms of the number of events vs the number of triggered ADC channels. These histograms allowed us to observe noise (a peak for less than about 275 triggered ADC channels) and saturation (another peak, but smaller, for more than about 4275 triggered ADC channels).
The thresholds for the number of selected strips and for the previously mentioned ratios were chosen in order to eliminate dark count events that mostly showed up at the image corners. After applying this optimization, we managed to eliminate most of the distortion present in Figure 10. The image is much more clearer and the events are now more concentrated on the letters and on the pictogram, as it is expected.

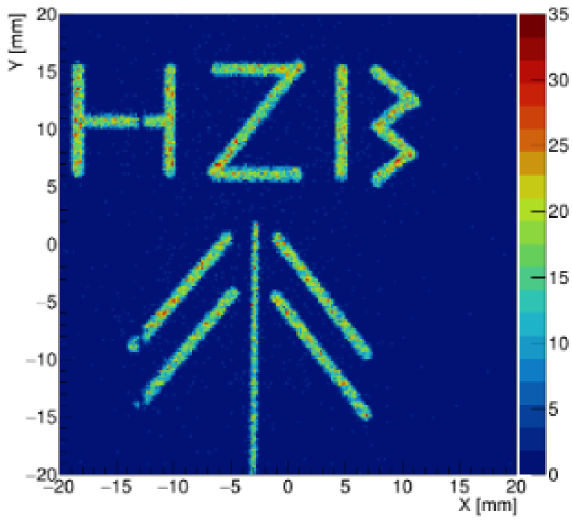

Figure 11. Reconstructed image obtained using an optimized centroid approach (N = 4; 200 x 200 bins).

5.4 Statistical Method

The idea of this method is to predict the strip signals corresponding to a certain event position using a numerical model and then compare them with the actual (recorded) signals. The method "sweeps" an area where the event could have taken place, and the position giving the best match in the signals is then the event position.
To achieve that, we use a type of function that describes the dependence of the strip signal on the lateral distance (distance between the event position and the centre of the strip). This function is called Strip Response Function (SRF).
We are obviously looking for the best possible match between the actual signal and the signal predicted using the SRF. For that we use a SRF that is known [5] to be the most appropriate, for the case of our detector:

$$SRF_i(x) = \frac{A}{cosh(W(x - x_i))} \quad (2)$$

with A being a scaling factor, W a width factor and x_i the coordinate of the centre of the strip i.
Knowing this, the method is started with a selection of the strips to perform the fitting with. The maximum signal strip and three on each of its sides are selected. Just as in the optimized centroid method, if the signal of a selected strip is below 20 triggered ADC channels, the strip is not included in the fit. Then, the selected signals and the corresponding strip position are fitted according to equation (2) and the obtained x value from this fit gives the event position. The events are again filtered based on the cathode signal (using the same exact values as before). The value of W is also used to decide whether or not the event should be discarded: if $1 < W < 5$ the event is not rejected.
Finally, the chi-squared of the fit is also determined. For X positions, an acceptable value of the chi-squared is between 0.2 and 100. For Y positions, the acceptable value is between 0.2 and 80 [5]. The final result appears on Figure 12.

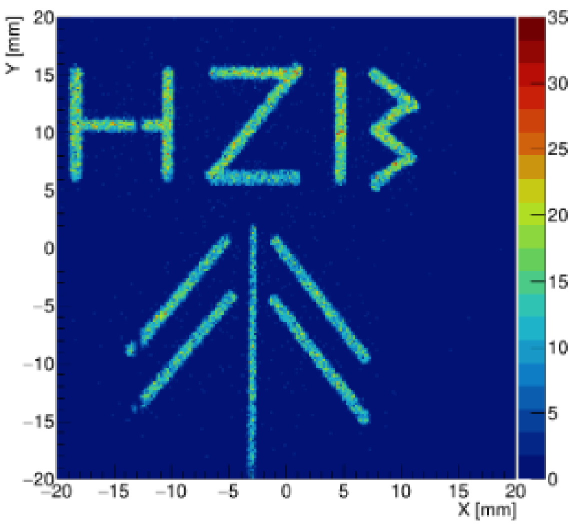

Figure 12. Reconstructed image obtained using the statistical approach (200 x 200 bins).

The result obtained using the optimized centroid method and the statistical one is similar but the latter is known to provide better image linearity and spatial resolution [5]. The main drawback is the fact that the Statistical method has higher computational costs.

6 Simulations

In this section, it is described the steps our internship group went through when doing simulations for optimizing the neutron detector in terms of detection efficiency and counting rate. The group was involved in beta-testing a new simulation toolkit, ANTS3, that was being developed by supervisor Andrey Morozov. ANTS3 makes use of GEANT4 which is a toolkit for Monte-Carlo simulation of passage of particles through matter [6].

6.1 Simulation Model

For the simulations that will be described in the next few subsections, a simplified version of the 10-Double Gap RPC Detector was used as the simulation model. It was composed of only one Double-Gap RPC. This RPC was made of, in order, an anode, a gas gap, a converter, a cathode, another converter, another gas gap and finally another anode. The anodes were made of Soda Lime Glass; The gas used in the gas gaps was freon; The material of the converters was $^{10}B_4C$; The cathode was made of aluminium.

6.2 Detection Efficiency vs angle of incidence

This simulation was done in order to get values of detection efficiency (DE) across a range of angles that define the direction of the neutron incidence on the detector (0º signifies that the beam is parallel to the RPC surface).
The minimum angle of incidence was chosen to be 5º due to the practical limits. For this simulation, fixed values of the neutron beam energy (25 meV) and the converter thickness (1.15 µm) were used.
In Figure 13, the result of this simulation can be seen. There is a strong decrease of the detection efficiency with the angle of incidence. This means that the best efficiency can be obtained for the smallest angle possible to achieve in the prototype. In this case, for 5º, a DE of 43% was achieved whereas for 90º, it was only 7%.

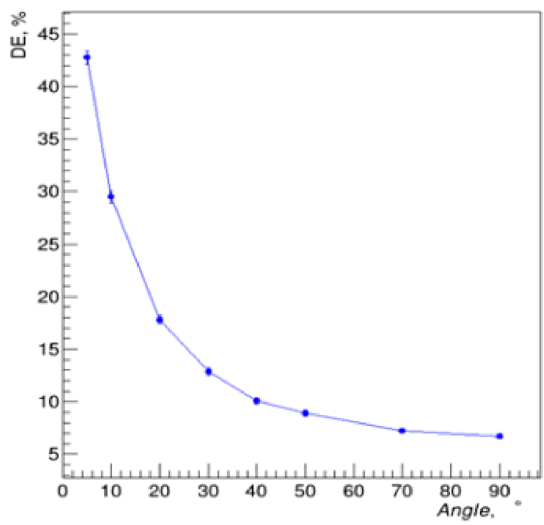

Figure 13. Detection Efficiency as a function of neutron beam angle of incidence. 90º is the normal incidence. Converter thickness was kept at 1.15 µm. Beam energy is 25 meV.

6.3 Detection Efficiency vs converter thickness

A simulation was also made to find the optimal converter thickness. As before, the neutron beam energy was fixed

at 25 meV. The angle of incidence of the beam was fixed for this simulation at 5º.
The result for this simulation can be seen in Figure 14. A rapid increase in detection efficiency can be seen until a peak is found at 1.15 µm. Following the peak, there is a decrease until around 5 µm explained by the ranges of the $^{10}B_4C$ particles. These ranges are short so some of the fission fragments would not deposit sufficient amounts of energy on the gas gap when the converter thickness increases. Above 5 µm only fragments with very high energies would be detected causing a constant DE value. This made DE to be constant starting at that converter thickness. For the peak, DE was 42%, whereas for the large thickness values it is 33.5%.

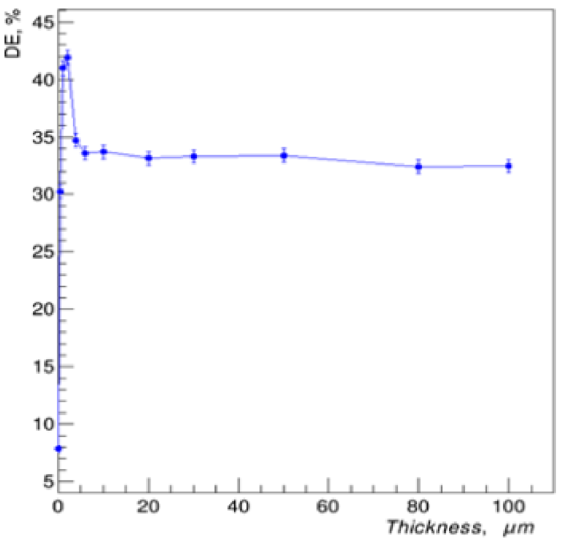

Figure 14. Detection Efficiency as a function of thickness of the converter. Orientation was kept at 5º. Beam energy at 25 meV.

Our group also simulated how the optimal thickness changes with the angle of incidence. Figure 15 suggests that at 5º the optimal thickness is 1.15 µm. However, the optimal converter thickness increases with the angle of incidence. For example, at 90º, the optimal thickness is between 2.3 and 3 µm.

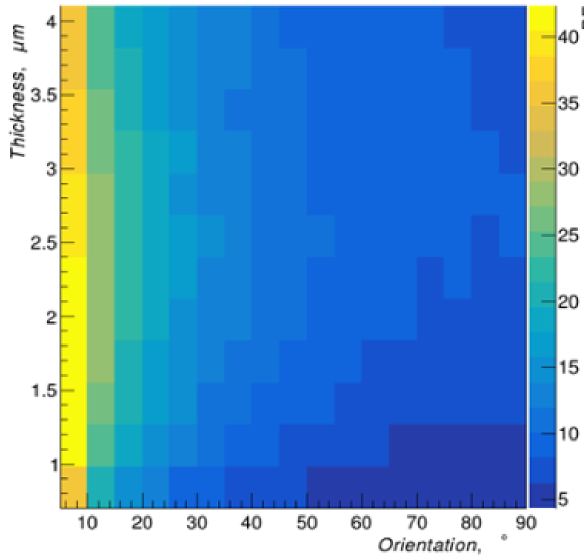

Figure 15. Heatmap of the detection efficiency as a function of neutron beam angle of incidence and thickness of the converter. Energy of the neutron beam was kept at 25 meV.

6.4 Detection Efficiency: total and only for non-scattered neutrons

Finally, another simulation was done that compared two detection efficiencies: one taking into account all neutrons and the other one considering only those neutrons which did not have elastic scattering before detection. This simulation was different from the others since it was also used to check if ANTS3 would give the same values using three different methods of extraction the detection efficiency. For the three methods, in order for an event to be considered as detected, the total amount of the deposited energy by the reaction products for that specific event had to be above a threshold of 100 keV. The first method made use of the ability of ANTS3 to use calorimeter data to get the detection efficiency for all neutrons. The second one was done by using the graphical user interface. It was able to automatically separate the detection events with prior scattering from those that had no scattering. The final method used was based on detailed analysis of the particle transport history. Our group created a script using Python or Javascript that, as for the second method, could check whether each event had prior scattering or not and calculate the amount of energy deposited in the detector. If this energy was above the threshold, the event was considered to have been detected and the detection efficiency for the simulation was obtained.
As it can be seen in Figure 16, the three methods give matching results. For 5º, we can see a small difference between both cases – around 1.5%. Comparing the middle and lower figures, it is visible that when increasing the angle of incidence, the ratio of DE for both scattered and non-scattered neutrons together over only non-scattered neutrons is maintained at 1.03.

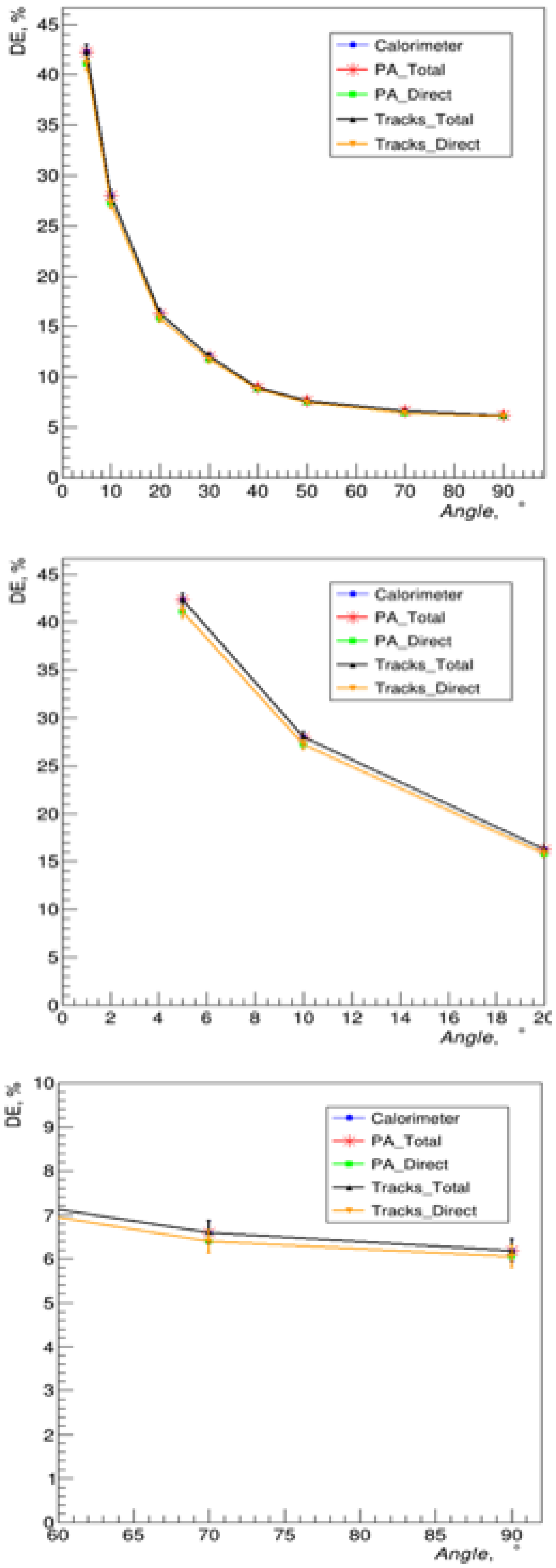

Figure 16. Detection efficiency as a function of neutron beam angle of incidence for both non-scattered and scattered neutrons and only for non-scattered neutrons using three different ANTS3 methods. Energy was kept at 25 meV. **Upper figure**: Neutron beam angle of incidence between 0º and 90º. **Middle figure**: Zoom in for angle of incidence between 0º and 20º. **Lower figure**: Zoom in for angle of incidence between 60º and 90º.

7 Conclusions

Working with the Neutron Detectors group at LIP, our laboratory and computing skills were improved. In the laboratory section of the internship, it was explained how the 10 Double-Gap RPC Detector was built and the Front-End Electronics were installed. Afterwards, it was explained how the DAQ system was used to retrieve the detector data in order to be able to do the image reconstruction. This part was concluded by checking if all the Front-End boards were working correctly and giving the correct results by calibrating the cathode channels. By doing this calibration, it was verified that all the cathodes FEE channels showed comparable sensitivity.
For the computing section of the internship, we performed a X and Y reconstruction of the position of neutrons that allowed us to retrieve the image of the mask put in front of the detector window. Simulations were also performed to check both the optimal thickness of the convertor and optimal incidence angle of the neutron beam. These were important since in the future if there is an intention to build a prototype detector, there is the need to know how to do different simulations in order to optimize the detector more easily. By doing these simulations we also participated in the beta-testing of the new software toolkit, ANTS3.

Acknowledgements

We would like to thank LIP and its staff for this opportunity and the warm reception that we were given, in particular our supervisors, Luís Margato and Andrey Morozov. Throughout this project we had the opportunity to get experience in high level physics investigation.
Thanks to Beatriz Lopes for allowing the usage of the contents of this document to illustrate the template.

References

[1] M. L.M.S., M. A., JINST (2018)
[2] M. et al. L.M.S., JINST (2020)
[3] A.N. et al., JINST (2013), [Online]
[4] TRB, *FaRICH1 System*, http://trb.gsi.de/ (2023), [Online]
[5] A.M. et al., JINST (2021)
[6] CERN, *GEANT4*, https://geant4.web.cern.ch/about/ (2023), [Online]